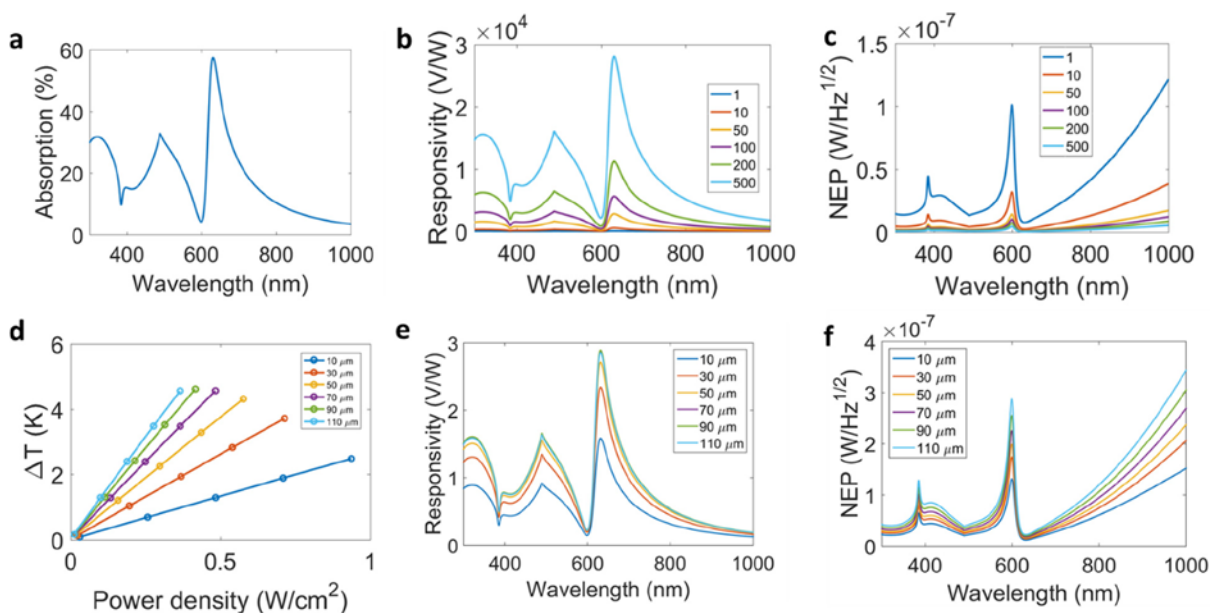


In the format provided by the authors and unedited.

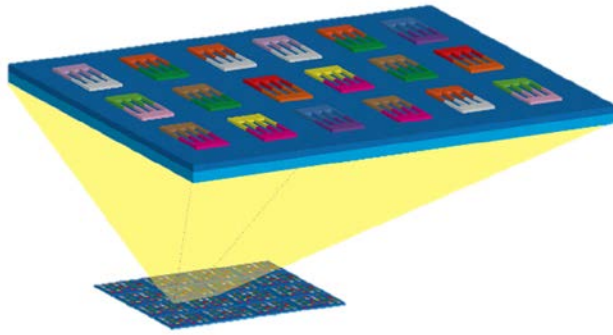
Resonant thermoelectric nanophotonics

Kelly W. Mauser, Seyoon Kim, Slobodan Mitrovic, Dagny Fleischman, Ragip Pala, Keith Schwab, and Harry A. Atwater

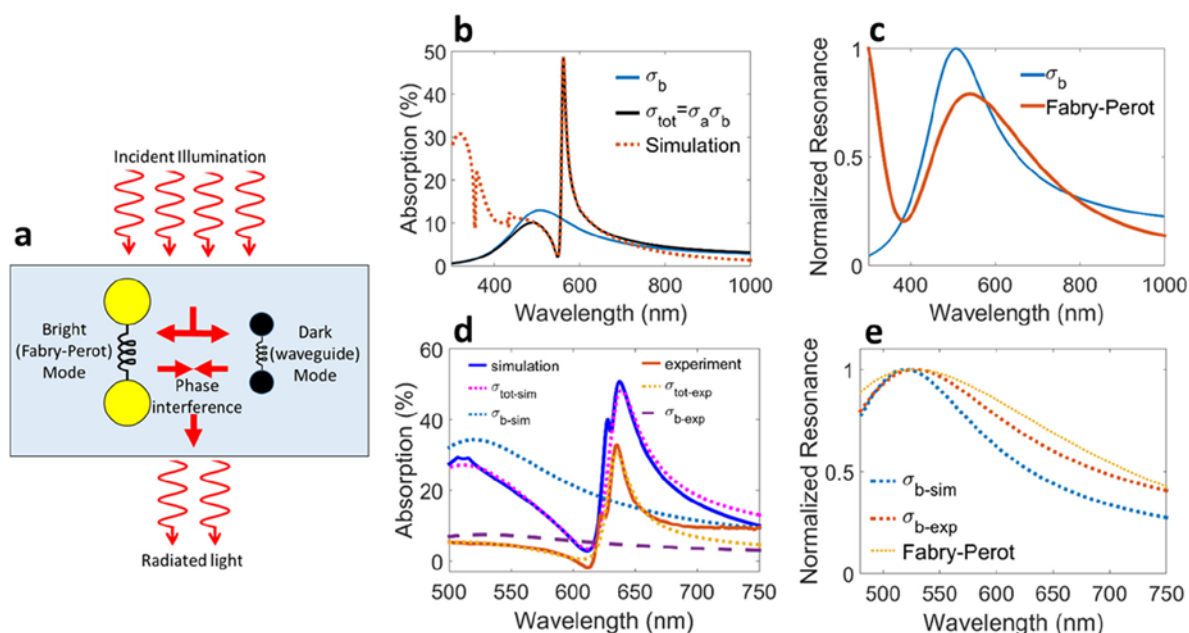
Supplementary Notes



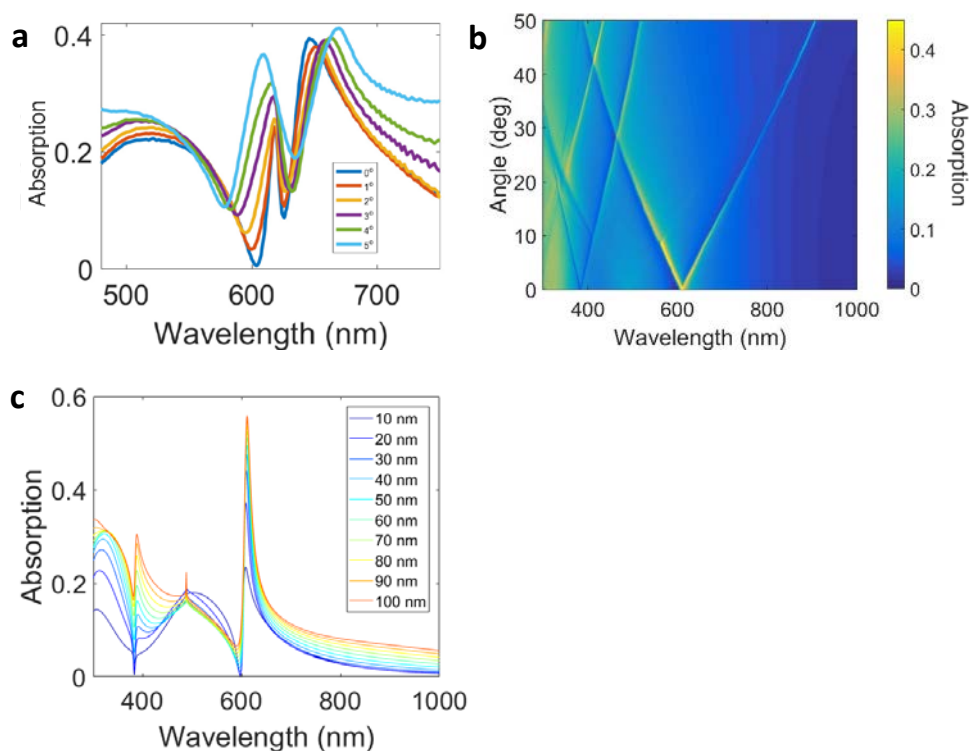
Supplementary Figure 1 | Thermopile and wire length analysis. **a**, Absorption spectra used in simulations for **b,c,e,f**. **b**, Responsivity for a structure with 50 μm long wires and 27 μm long pads, as a function of number of wires in a thermopile configuration. The entire structure is illuminated and responsivity is calculated relative to power striking the wire area. The pads are assumed to have a 20% absorption, independent of wavelength. **c**, Noise equivalent power (NEP) for the thermopiles in **b**, assuming Johnson noise as the noise spectral density using simulated average temperatures. **d**, Temperature difference between the edge of the pad and the center of the wires versus power density for different wire lengths. Pad sizes remain constant with dimensions of 50 μm by 27 μm by 50 nm. **e**, Responsivity as a function of wavelength for the absorption spectrum in **a**, for different wire lengths, relative to power illuminating the entire structure. **f**, Noise equivalent power corresponding to the responsivity in **e**, for different wire lengths. Noise spectral density is theoretical Johnson noise using simulated average temperatures for the structures. Simulation details are given in Supplementary Note 1.

**Supplementary Figure 2 | Conceptual design of hyperspectral pixel.**

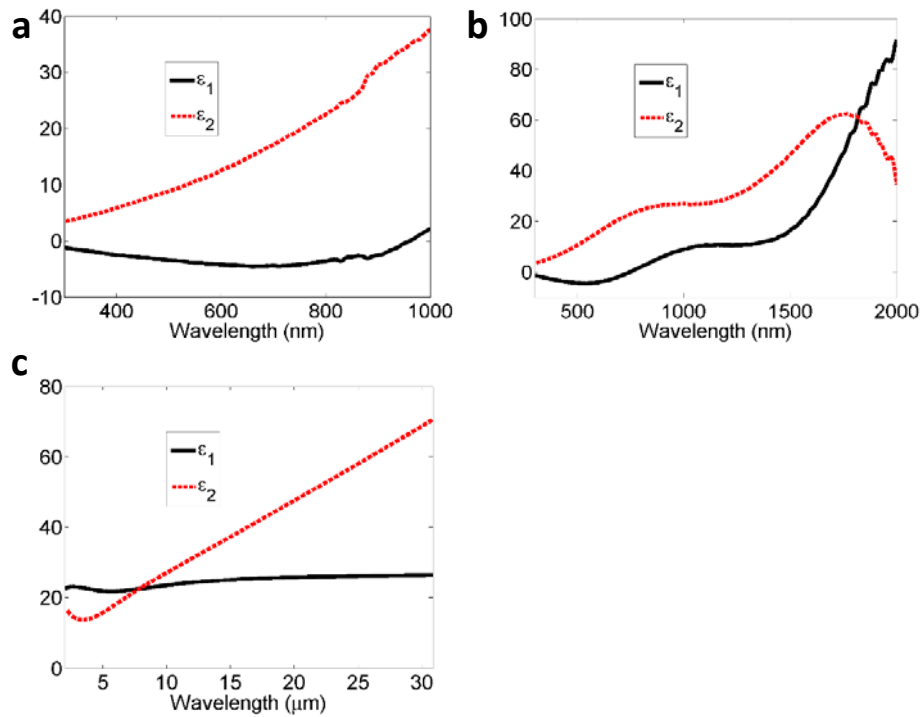
Each thermoelectric structure in the pixel has a different wire pitch, causing each structure to have an absorption peak that corresponds to a different wavelength (Fig. 3). When light of unknown wavelength content illuminates the pixel, voltages will be produced in each structure depending on their specific absorption profiles. Deconvolution of these voltage signals through an algorithm can enable identification of the unknown wavelengths.



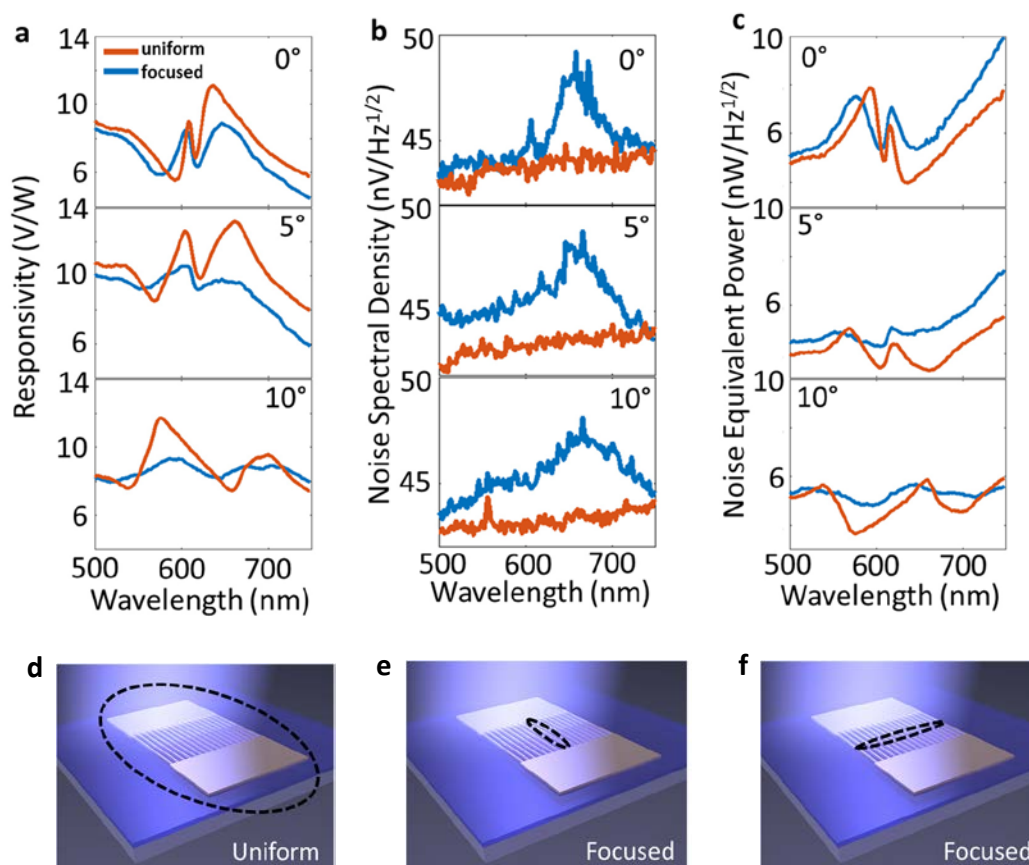
Supplementary Figure 3 | Fano resonance analysis. **a**, Diagram of interaction of bright (broad resonance) and dark (narrow resonance) modes in the production of Fano lineshapes. The bright mode is the Fabry-Perot resonance of light with k -vector parallel to incident illumination. Analysis from Gallinet et al.¹ **b**, Full wave simulation of Sb_2Te_3 wires that are 60 nm wide, 40 nm thick, with a pitch of 431 nm on a 50 nm SiO_2 /100 nm SiN_x suspended waveguide, that is fit to the Fano formula (Supplementary equation (S6)). Shown are the simulation (dotted orange), the fit to the combined Fano formula (black, Supplementary equation (S6)) between 440 nm and 650 nm, and the extracted Fano formula of the bright mode (blue, Supplementary equation (S5)). **c**, The Fabry-Perot resonance (orange) is calculated via full-wave simulation as the normalized magnitude of the electric field at a point on the surface of a bare waveguide structure. The bright mode fit (blue) is described in **b**. The shift in the Fabry-Perot peak is associated with the contributions of the wires to the effective index of the entire photonic crystal structure. **d**, Experiment versus simulation for 45 nm SiO_2 /100 nm SiN_x suspended waveguide with Sb_2Te_3 wires. Wire thickness is 40 nm, width is 89 nm, and pitch is 511 nm. Shown are the full wave simulation for this structure (solid blue), the total Fano function fit (dotted magenta) to the full wave simulation with parameters given in Supplementary Table 2, and the bright mode (dotted blue) extracted from the total Fano fit function, corresponding to the Fabry-Perot resonance. Also shown are the measured absorption (solid orange), the fitted total Fano function to the measured absorption (dotted yellow), and the extracted bright mode profile from the measured extinction (dashed purple). **e**, Extracted bright mode for the experimental (dotted orange) and simulated (dotted blue) data from **d**, with the simulated electric field magnitude (dotted yellow) at the surface of the waveguide (without the wires) due to the Fabry-Perot resonance. All curves are normalized to their maximum value in the given wavelength range for ease of comparing resonance peaks. The experimental, simulated, and Fabry-Perot peaks align reasonably well.



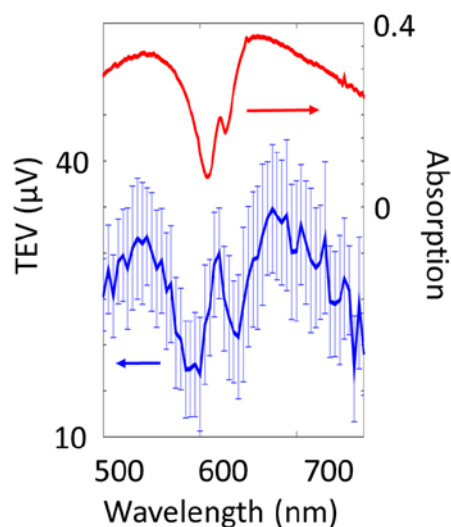
Supplementary Figure 4 | Dependence of absorption spectra on incident illumination angle and wire thickness. **a**, Measured absorption spectra for different angles of incidence. An objective with numerical aperture 0.14 was used, giving an angular spread even at normal incidence, producing the side peak at normal (0°) incident angle. **b**, Full wave simulations of the incident illumination angle dependence of 40 nm tall, 67 nm wide Sb_2Te_3 wires with a pitch of 488 nm on a 50 nm SiO_2 on 100 nm SiN_x waveguide. Even at 1 degree offset, the single peak splits into two. **c**, The dependence of wire thickness on absorption spectra, with pitch of 488 nm. The absorption asymptotes to its maximum value for wire heights around 40 nm.



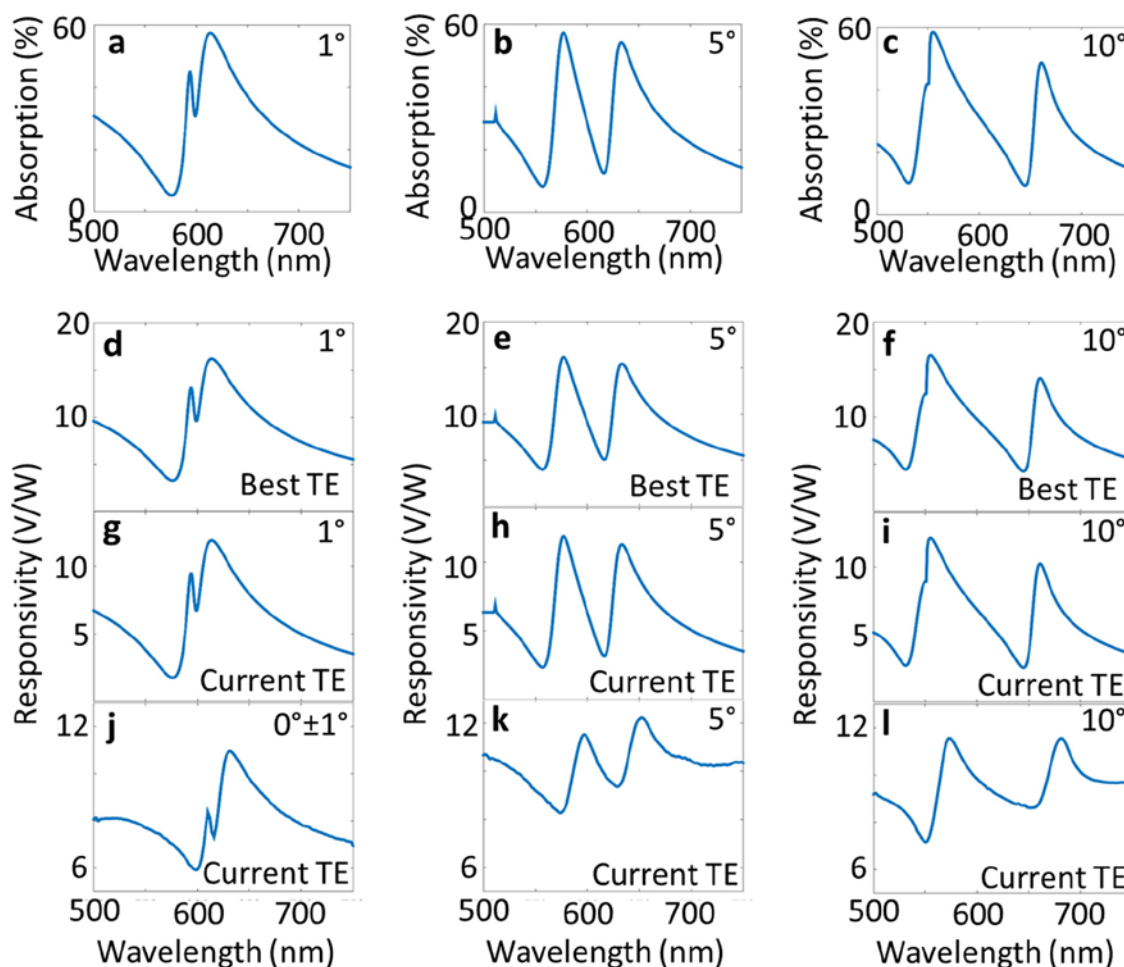
Supplementary Figure 5 | Thermoelectric dielectric functions. a,c, Dielectric functions of Bi_2Te_3 from 300-1000 nm (a) and 2-31 μm (c). b, Dielectric function of Sb_2Te_3 from 300-2000 nm.



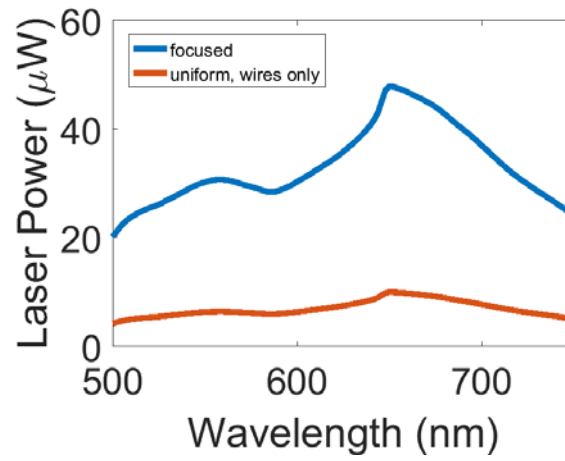
Supplementary Figure 6 | Focused versus unfocused, spatially uniform light responsivity and noise characteristics. Focused (blue, 60 μm by 5 μm spot size, **e**) and unfocused, spatially uniform (orange, 120 μm by 100 μm spot size, **d**) illumination incident on $\text{Bi}_2\text{Te}_3\text{-Sb}_2\text{Te}_3$ structures at given angles off normal incidence, with $\pm 1^\circ$ error. A 5 \times objective with numerical aperture 0.14 was used for both the focused and spatially uniform illumination data collection. **a**, The input power used to calculate responsivity in the case of uniform illumination was only the power that illuminated the wires (a $50 \times 50 \mu\text{m}^2$ area). The spatially uniform illumination spot was 120 μm by 100 μm , and completely covered the wires and pads of the structure. Noise spectral density, **b**, was measured under the power spectrum shown in Supplementary Fig. 9. Higher noise spectral density in focused light was likely due to back currents from uneven heating in the structure, discussed further in Supplementary Note 6. **c**, Noise equivalent power was found to be lower for spatially uniform illumination than for focused illumination, due to higher responsivity values combined with lower noise values for spatially uniform illumination. **d**, Black circle illustrates uniform illumination of structure. **e**, Focused illumination used in **a-c**, Fig. 4d. **f**, Focused illumination in Fig. 4c.



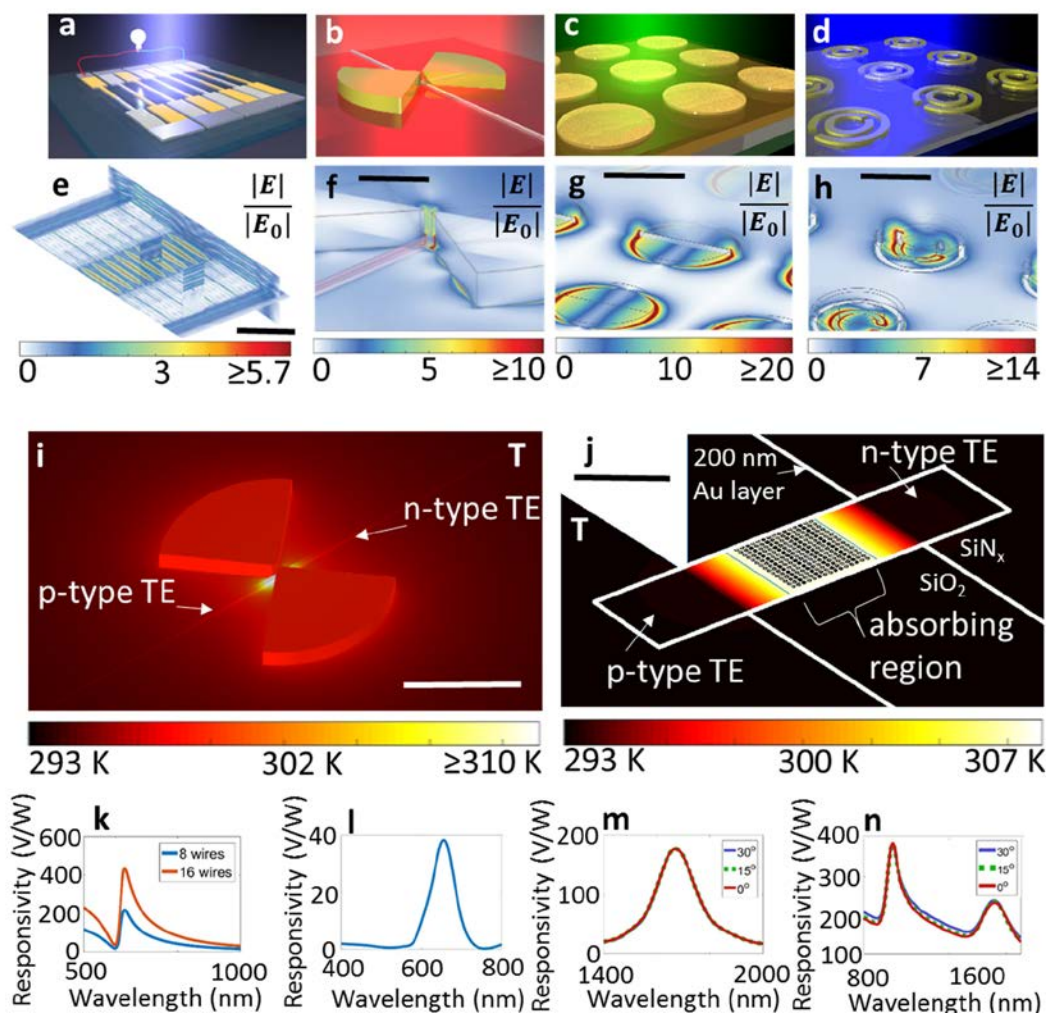
Supplementary Figure 7 | Chromel-alumel structure results. Thermoelectric potential (TEV) and absorption results for a chromel-alumel structure with the same dimensions as that of the $\text{Bi}_2\text{Te}_3\text{-Sb}_2\text{Te}_3$ structures. The structure is under $70.92 \mu\text{W}$ illumination, or 30.4 W/cm^2 incident power density. Data points are taken as the focused beam is moved across the junction of the detector (over a $\sim 400 \mu\text{m}^2$ area). All data points are averaged together for a given wavelength.



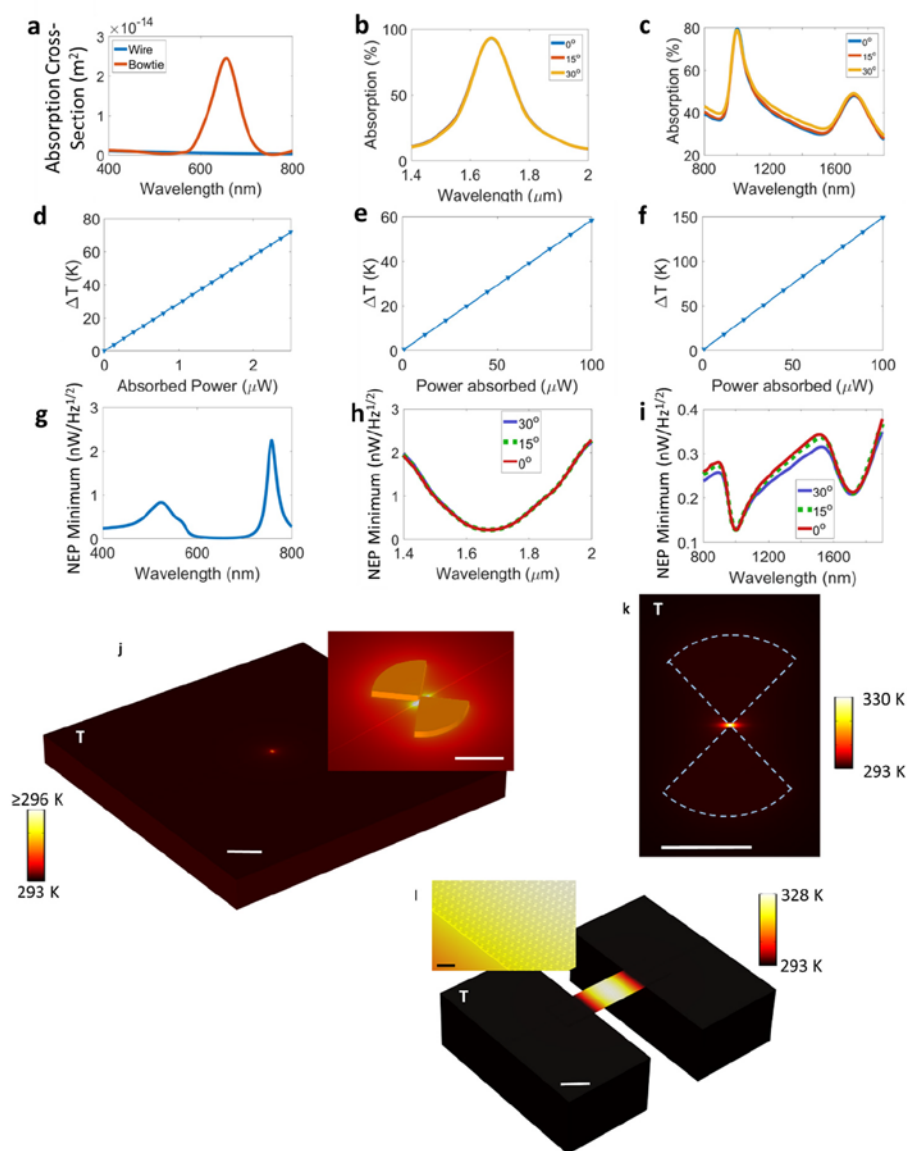
Supplementary Figure 8 | Responsivity from thermal simulations with current and state-of-the-art thermoelectrics. **a-c**, Simulated absorption spectra for wires of the dimensions of the experimental Bi_2Te_3 - Sb_2Te_3 structures at 1, 5, and 10 degrees off normal incidence. **d-l**, Responsivity calculated from thermal simulations using absorption to guide power input at different angles off normal incidence. 20% absorption in the pads was assumed independent of wavelength. Simulated absorption from **a-c**, thermal properties and Seebeck coefficient of state-of-the-art thermoelectric materials, given in Supplementary Note 10, were used in **d-f**. Simulated absorption from **a-c**, thermal properties given in Supplementary Note 1 and average Seebeck coefficient of our materials ($242 \mu\text{V/K}$ for Sb_2Te_3 and $-84 \mu\text{V/K}$ for Bi_2Te_3 , see Supplementary Note 8) was used in **g-i** to calculate responsivity. Experimental absorption from Fig. 4a, thermal properties from Supplementary Note 1 and average Seebeck coefficient of our materials (above) was used in **j-l** to calculate responsivity. Details of thermal simulations are given in Supplementary Note 1.



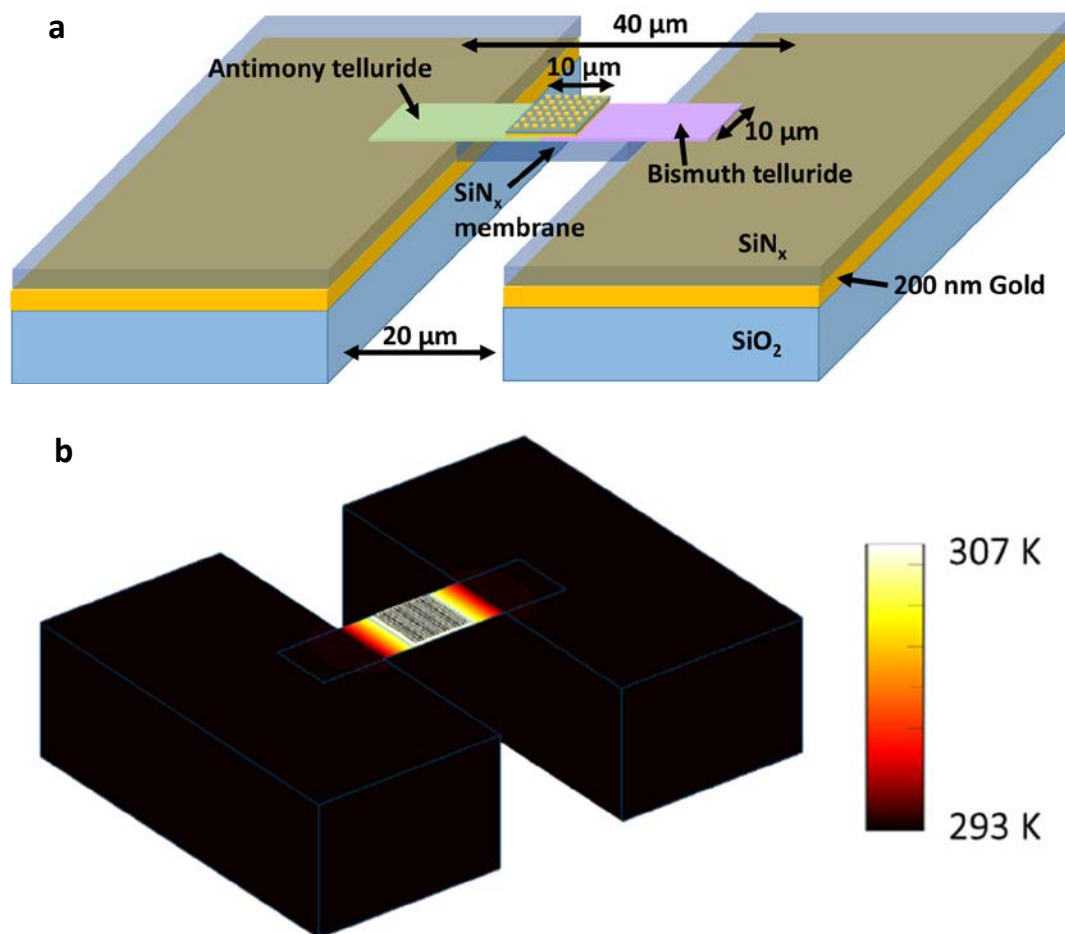
Supplementary Figure 9 | Laser power on wires. Laser power illuminating the wire region as a function of wavelength for focused illumination (blue) and uniform illumination (orange).



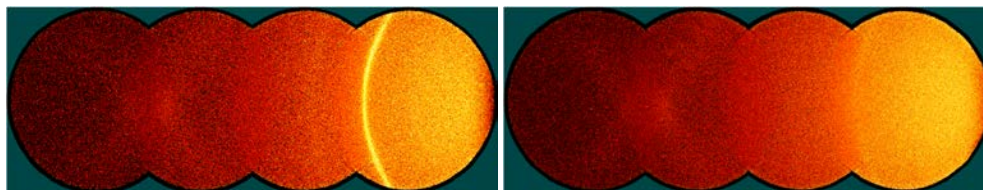
Supplementary Figure 10 | Resonantly excited nanophotonic thermoelectric structures. **a-d**, Conceptual images of the guided mode resonance structures in a thermopile configuration (**a**), a gold resonant bowtie antenna focusing the electric field on a thermoelectric wire junction (**b**), a perfect absorber design on top of a thermoelectric junction (**c**), and a split ring resonator absorber with a thermoelectric junction as a backreflector (**d**). **e-f**, Full wave simulations of the structures above, with electric field $|E|$ normalized by incident electric field $|E_0|$. Excitation wavelengths are 631 nm, 660 nm, 1,648 nm, and 1,710 nm, respectively. Scale bars for **e-f** are 2 μm , 200 nm, 300 nm, and 50 nm, respectively. **i,j**, Thermal simulations of the resonant bowtie antenna and perfect absorber design, respectively. The perfect absorber array covers a 10 μm by 10 μm square in the center of a suspended, thermoelectric junction on top of a SiN_x membrane. The “cold” ends of the thermoelectric materials sit on a 100 nm SiN_x/200 nm Au/20 μm SiO₂ substrate. The Au layer acts as a high thermal conductivity heat sink to conduct heat away from the “cold” ends of the thermoelectric materials. Both simulations were performed in vacuum. The scale bars in **i,j**, are 500 nm and 10 μm , respectively. The absorbed power in **i,j**, are 7.9 μW and 23 μW , respectively. More details can be found in Supplementary Note 1,11 and Supplementary Figs. 11,12. **k**, Simulated responsivity of the thermopiled thermoelectric structure shown in **a,e**, for 8 and 16 wire thermoelectric junctions in series. More details can be found in Supplementary Fig. 1. **l**, Simulated responsivity of the resonant bowtie absorber. **m,n**, Simulated responsivities as a function of incident angle of the perfect absorber and split ring resonator absorber, respectively. Further details for calculations of **l-n** can be found in Supplementary Fig. 11. In **k-n**, the combined Seebeck coefficient of the thermoelectric materials is assumed to be 326 $\mu\text{V/K}$.



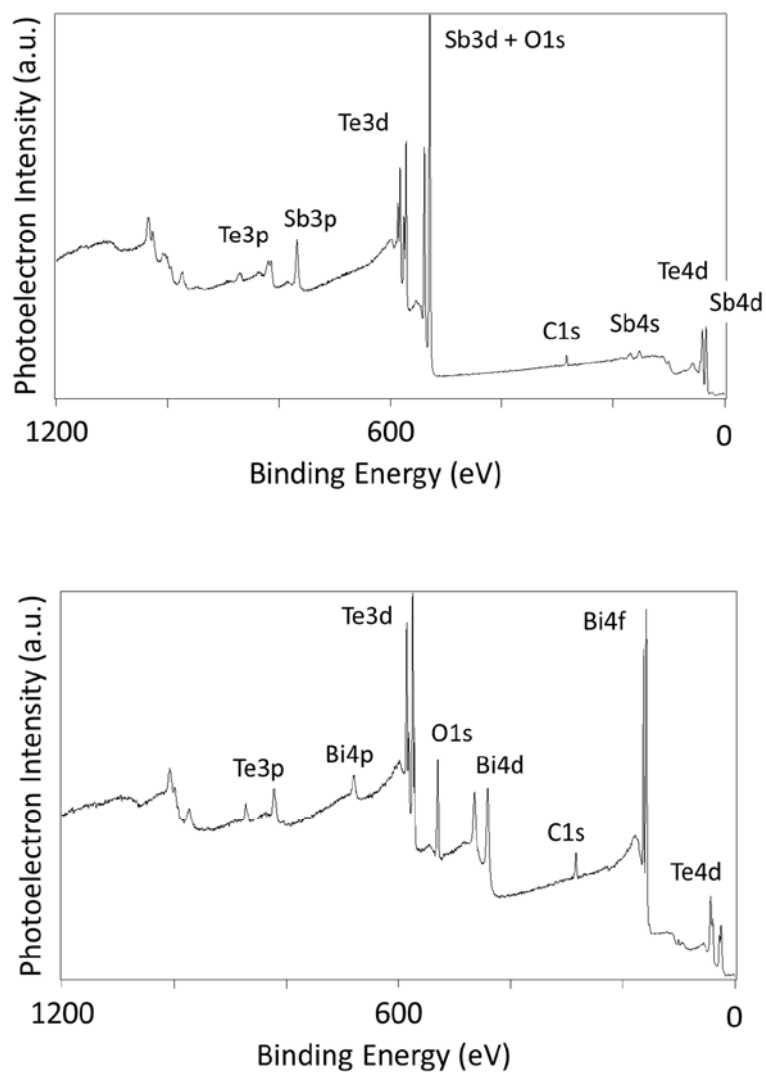
Supplementary Figure 11 | Bowtie and other absorber designs. **a,b,c** Absorption cross-section or absorption for the resonant bowtie absorber, perfect absorber, and split ring resonator absorber described in Supplementary Note 1. **d,e,f** Temperature differences between the hot and cold sides of the thermoelectric materials as a function of power absorbed for the bowtie, perfect absorber, and split ring resonator absorber described in Supplementary Note 1. **g,h,i** Noise equivalent power (NEP) lower bound as a function of wavelength for the bowtie, perfect absorber, and split ring resonator absorber described in Supplementary Note 1. Details of calculations are given in Supplementary Note 1. Briefly, responsivity results are shown in Supplementary Fig. 10k-n, and noise spectral density is calculated using theoretical Johnson noise, assuming the measured resistivity of our Bi_2Te_3 and Sb_2Te_3 materials at room temperature. **j**, Thermal simulation of bowtie structure with absorbed power of $7.9 \mu\text{W}$. Maximum temperature is $\sim 330 \text{ K}$, but a smaller scale was used to show temperature differences better. Scale bar is $20 \mu\text{m}$ and inset scale bar is 500 nm . **k**, The same thermal simulation as in **j** is shown, but with the full temperature scale bar. The outline of the bowtie is given in blue dotted line. Scale bar is 500 nm . **l**, Thermal simulation for split ring resonator perfect absorbers utilizing a thin membrane to lower thermal heat loss to the substrate. Total absorbed power is $23 \mu\text{W}$. Scale bar is $10 \mu\text{m}$. Further details are given in Supplementary Note 1 and Supplementary Fig. 12.



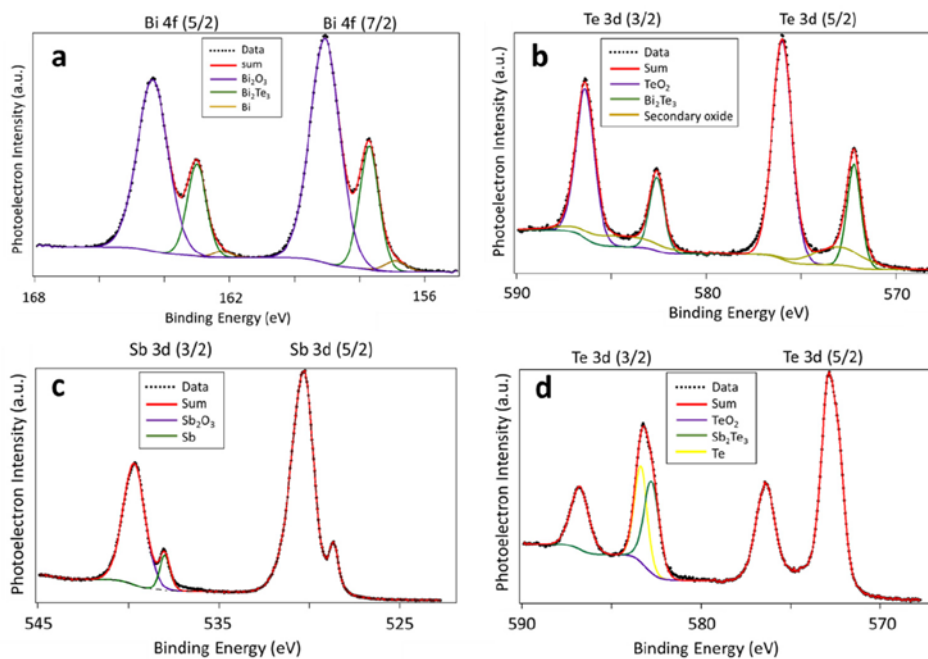
Supplementary Figure 12 | Perfect absorber and split ring resonator thermal simulation design. **a**, Diagram of thermal simulation design for a perfect absorber and a split ring resonator thermal simulation corresponding to data in Supplementary Fig. 10j,m,n and Supplementary Fig. 11e,f,h,i,l. The split ring resonator design has a 50 nm thick SiN_x membrane with 60 nm of thermoelectric material above it, which serves as a backreflector in the optical design. The perfect absorber has a 100 nm thick SiN_x membrane and 100 nm thick TE materials. It uses a 50 nm thick layer of gold as the backreflector in the 10 μm by 10 μm center absorber patch. The 200 nm gold above the silica increases thermal conduction of heat from the cold end of the device (i.e. acts as a heat sink), and any other thermally conductive material would serve this purpose well. Thermal simulations involved a volumetric heat influx into the centrally located SRR or cylinder absorbers in the array (this assumes absorption near the edges of the arrays would be worse). **b**, Thermal simulation of perfect absorber with a total absorbed power of 23 μW . The split ring resonator thermal profile was similar (see Supplementary Fig. 11l).



Supplementary Figure 13 | XRD data. XRD data of 100 nm of Bi₂Te₃ (left) and 50 nm Sb₂Te₃ (right) show very little crystallinity, as sputtered in experiments. Two-dimensional diffraction image frames were collected with frame centers set to 20, 40, 60 and 80 degrees in 2 Θ , from right to left, and then merged.



Supplementary Figure 14 | XPS survey scans. Sb_2Te_3 (top) and Bi_2Te_3 (bottom) samples.



Supplementary Figure 15 | Compositional analysis. Detailed XPS data and fits for bismuth telluride peaks (a-b) and antimony telluride peaks (c-d) for our samples. **a**, Three components are visible in Bi 4f levels: the major components are Bi₂O₃, and Bi₂Te₃ (157.1 eV and spin-orbit pair at + 5.3 eV), with a small amount of elemental bismuth (156.6 eV). **b**, Te 3d level in bismuth-telluride is mostly TeO₂ and Bi₂Te₃ (582.3 eV, SO-splitting of 10.4 eV). **c**, Sb 3d levels show that most of the surface of antimony-telluride is oxidized (Sb₂O₃), much more so than the bismuth-telluride, with a measurable Sb₂Te₃ component (538 eV). **d**, Te 3d levels in antimony-telluride show the telluride, an oxide and elemental Te peaks.

Supplementary Table 1. Comparison of experimental dimensions and illumination angle ($Pitch_s$, $Width_s$, Θ_s) with best-fit simulation dimensions, illumination angle ($Pitch_f$, $Width_f$, Θ_f) and scaling factor corresponding to Fig. 3d in the main text.

Absorption curve	$Pitch_s$ (nm)	$Width_s$ (nm)	Θ_s (deg)	$Pitch_f$ (nm)	$Width_f$ (nm)	Θ_f (deg)	Scaling
i	567	97	0.5	560	97	0.5	0.71
ii	566	91	0.5	560	90	0.5	0.66
iii	511	119	0.5	507	102	0.6	1.06
iv	509	98	0.5	507	87	0.6	0.87
v	511	89	0.5	507	82	0.6	0.76
vi	452	131	1	455	102	1	0.99
vii	452	101	1	455	87	1	0.87

Supplementary Table 2. Fitting parameters for Supplementary equation (S6) for Supplementary Figs. 3. 95% confidence intervals are given.

Figure	a (unitless)	ω_a (eV)	W_a (eV)	ω_b (eV)	W_b (eV)	q (unitless)	b (unitless)
S4/S5	0.13038 ±	2.2174 ±	0.020862 ±	2.4448 ±	0.48832	-1.6986 ±	0.82025 ±
	0.000704	0.00014	0.000133	0.0067	± 0.00726	0.00943	0.0388
S6/S7 – simulation	0.58557 ±	1.9725 ±	0.041887 ±	2.383 ±	0.38067	-1.2762 ±	0.53022 ±
	0.00514	0.000991	0.000941	0.0233	± 0.0203	0.0227	0.0578
S6/S7 – experiment	0.27396 ±	1.9637 ±	0.032595 ±	2.3473 ±	0.48954	-2.185 ± 0.11	0.6564 ±
	0.00968	0.00144	0.00151	0.0563	± 0.0991		0.412

Supplementary Table 3. Measured Seebeck coefficient of 6 different samples of thermoelectric material.

Sample	Seebeck coefficient ($\mu\text{V}/\text{K}$)
$\text{Sb}_2\text{Te}_3 - 1$	264 ± 16.6
$\text{Sb}_2\text{Te}_3 - 2$	214 ± 14.6
$\text{Sb}_2\text{Te}_3 - 3$	247 ± 15.9
$\text{Bi}_2\text{Te}_3 - 1$	-81 ± 3.1
$\text{Bi}_2\text{Te}_3 - 2$	-77 ± 3.9
$\text{Bi}_2\text{Te}_3 - 3$	-95 ± 5.2

Supplementary Table 4. Literature values of Seebeck coefficient and resistivity.

Citation	Material	Resistivity ($\Omega\cdot\text{cm}$)	Seebeck Coefficient ($\mu\text{V/K}$)	Details
Horne ²	Bi_2Te_3	2.7×10^{-4} to 1.71×10^{-3}	+160 to -145	bulk with oxide impurities
Böttner et al. ³	Bi_2Te_3	2.1×10^{-3}	-50	10 microns, sputtered
da Silva et al. ⁴	Bi_2Te_3	8×10^{-3}	-50	coevaporated, ~1 micron
Zou et al. ⁵	Bi_2Te_3	1.29×10^{-3} to 2.6×10^{-3}	-143 to -228	coevaporated, 700 nm
da Silva et al. ⁴	Sb_2Te_3	4×10^{-3}	+140	coevaporated, ~1 micron
Pinisetty et al. ⁶	Sb_2Te_3	x	+70 to +365	100 and 400 nm diameters. 100 nm amorphous gave $\alpha \sim +230 \mu\text{V/K}$
Baily et al. ⁷	Sb_2Te_3	1.11	+700, +800	amorphous, cosputtered, ~1 micron
Shi et al. ⁸	Sb_2Te_3	0.91	+125	hydrothermal synthesis
Zou et al. ⁵	Sb_2Te_3	1.04×10^{-3} to 4.90×10^{-3}	+140 to 171	coevaporated, 700 nm

Supplementary Note 1. Description of thermal simulations

The theoretical temperature spectrum found in Fig. 1b of the manuscript for the guided mode resonance wire structure was constructed as follows. Absorption data were taken from 2D periodic electromagnetic simulations and combined with experimentally measured power. The combined data was used as a volumetric input power source in a thermal simulation. Simulation sizes were large enough that changes in fixed boundary temperatures did not affect central temperature profiles. Due to memory constraints, symmetry boundary conditions were used, so simulations used one material, bismuth telluride, instead of both bismuth telluride and antimony telluride. Heat capacity of Bi_2Te_3 ⁹ was taken as 158 J/kg·K, density¹⁰ as 7,859 kg/m³, surface emissivity as 0.34, and thermal conductivity¹¹ as 2.05 W/m·K. SiN_x heat capacity¹² was taken as 800 J/kg·K, density as 3,185 kg/m³, surface emissivity as 0.9, and thermal conductivity¹³ as 2.5 W/m·K. SiO_2 heat capacity¹² was taken as 703 J/kg·K, density as 2,196 kg/m³, surface emissivity as 0.9, and thermal conductivity¹⁴ as 1.38 W/m·K. Au heat capacity was taken as 129 J/kg·K, density as 19300 kg/m³, surface emissivity as 0.025, and thermal conductivity as 317 W/m·K. Of course, while our thermal simulations were able to explain experimental results reasonably well (compare Fig. 4b and Supplementary Fig. 8j-l), it is known that small crystal grain sizes can decrease thermal conductivity in thin film BiTe-based materials¹⁵. From our XRD data (Supplementary Fig. 13), we can see that the grain structures must not be large. We recognize the bulk values of thermal conductivity used in our thermoelectric materials in the simulations may be different than that of our thin-film materials. Dimensions in simulations were the same as those of the fabricated sample: 40 nm tall wires and pads, 100 wires total, 50 μm long (25 μm for each thermoelectric material), with a pitch of 520 nm and wire width of 130 nm. The thermoelectric pad lengths were 27 μm and as wide as the wire array. The Au contacts were 6 μm wide and 70 nm tall, and overlapped the pads by 5 μm .

The bowtie (Supplementary Fig. 10b,i) simulated had an internal angle of 90 degrees and were cut from a circle of radius 500 nm and thickness 80 nm. The gap between the “wings” of the bowtie was 30 nm. The wire was 20 nm wide and 20 nm tall and made of one material, bismuth telluride, due to memory and symmetry constraints. The bowtie was gold with index of refraction from Palik¹⁶. The substrate was an infinitely thick slab of SiO_2 with index of 1.455. The thermal simulation was conducted as with the guided mode resonance structure, with

thermal properties for materials described above, and results are shown in Fig. 5i and Supplementary Fig. 13d,j,k.

The perfect absorber design was modeled off a design from the literature¹⁷. The cylinder height was 20 nm, the radius 176 nm, and the pitch 600 nm. The dielectric gap was 30 nm thick SiO₂ with index from Palik¹⁶. The backreflector was 50 nm gold with index data from Johnson and Christy¹⁸, beneath which was 100 nm of bismuth telluride (see Supplementary Fig. 5 for measured dielectric functions). In the thermal simulations, a patch of the perfect absorber materials was placed in the center of the 100 nm thick thermoelectric junction on top of a 10 μm wide, 100 nm thick SiN_x membrane suspended between two large blocks of SiO₂, shown in Supplementary Fig. 12a and Supplementary Fig. 10j. Sandwiched between the large SiO₂ blocks and the “cold” end of the SiN_x membrane is a 200 nm thick layer of Au. Because Au has a large thermal conductivity, this layer acts as a heat sink for the “cold” end of the thermoelectric materials, enhancing the temperature gradient across the thermoelectric materials. The simulations neglected convection, i.e. simulated a vacuum environment.

The split ring resonator perfect absorber consists of two gold rings, the outer ring with outer radius 70 nm and inner radius 60 nm, with a split 15 nm wide. The inner ring had outer radius of 40 nm and inner radius of 30 nm, with split 20 nm wide. Both rings were 20 nm tall and had optical constants from Johnson and Christy¹⁸. From center to center, the distance between each split ring resonator in the array is 240 nm. The dielectric layer was 40 nm of Palik¹⁶ SiO₂. The backreflector layer was made of antimony telluride. The thermal simulations were performed in a similar manner as the perfect absorber structures described above, but with a 60 nm thick thermoelectric layer and 50 nm thick SiN_x membrane below. Further details are found in Supplementary Fig. 12, and simulation results can be found in Supplementary Fig. 11.

Simulations done in Supplementary Fig. 1 were performed in a similar manner to those described for the guided mode resonance wire structures above. The results of the wire simulations were also used in Supplementary Figs. 1b,c to approximated outputs of thermopile configurations. We find that increasing power density will linearly increase the difference in temperature between the “cold” edge of the thermoelectric pads and the junction at the center of the wires (Supplementary Fig. 1d). Relative to power impinging upon the entire structure, the responsivity of wires increases with length until 90 μm, then slightly decreases at 110 μm

(Supplementary Fig. 1e, average of measured Seebeck coefficients of $-84 \mu\text{V/K}$ (Bi_2Te_3) and $242 \mu\text{V/K}$ (Sb_2Te_3) used). We can explain the decrease in responsivity at $110 \mu\text{m}$ in the following way: while there is more area available to absorb light, and therefore more total power absorbed, this absorbed power is not localized on the thermoelectric junctions as much as the absorbed power in the smaller wire structures is. Because pad lengths are held constant, the larger wire area will simply heat up the entire structure, including the edges of the pads more. The maximum heat of the wires will increase, but the temperature of the “cold” ends will also increase, creating a smaller overall ΔT , and therefore a smaller voltage. Increasing the length of the pads would allow responsivity to increase with wire length for wires longer than $110 \mu\text{m}$. Using theoretical Johnson noise as our noise spectral density and using the measured resistivity of our materials and simulated temperature rises, we find that because of their overall higher resistances, longer wires will have higher noise equivalent powers. We chose to study structures with $50 \mu\text{m}$ wires as it gives a high responsivity with lower noise equivalent power.

Supplementary Note 2. Fano resonances

Fano lineshapes are produced when a continuum of states interacts with discrete or narrow modes near the same energy, and appear in electronic circuits, nanophotonics, and atomic spectra¹⁹. In our specific case, we have a broad, Fabry-Perot resonance in our waveguide layers acting as the continuum background (radiative bright mode), and a narrow, waveguide mode (nonradiative dark mode) interacting with it. The effect is developed thoroughly in work by Gallinet et al.^{1,19,20}, which will be summarized here.

From the interaction between the bright (continuum) and dark (waveguide) modes, as Supplementary Fig. 3a outlines, we get a new resonance of the combined system, at a position equal to

$$\omega_a^2 = \omega_d^2 + \omega_d \Delta, \quad (S1)$$

where ω_d is the resonant frequency of the dark mode and Δ is the shift away from this frequency due to coupling with the bright mode calculated explicitly in Gallinet¹⁹. The shape of the new resonance is asymmetric about the new resonance, ω_a , and is given by

$$\sigma_a(\omega) = \frac{\left(\frac{\omega^2 - \omega_a^2}{\Gamma} + q\right)^2 + b}{\left(\frac{\omega^2 - \omega_a^2}{\Gamma}\right)^2 + 1}, \quad (S2)$$

where q is an asymmetry term, Γ is a width term equal to $2\omega_a W_a$ (W_a is a width) for $\omega_a \gg W_a$, and b is a modulated damping term¹⁹. The asymmetry of this dark mode comes from a rapid phase asymmetry of $\sim\pi$ across the resonance from the original dark mode, interfering with the symmetric phase difference in the bright mode across the resonance. On one side of the resonance, these bright and dark modes destructively interfere, and on the other side of the resonance they constructively interfere. The location of destructive interference on either side of the resonance depends on the sign of the phase difference between the dark and bright mode resonances, along with whether the loss is real or imaginary. This is expressed in the asymmetry term in Supplementary equation (S2), q , where

$$q = \pm \frac{(\omega_d^2 - \omega_b^2)}{2\Gamma_b \left(1 + \frac{\Gamma_i}{\Gamma_c}\right)}, \quad (S3)$$

where Γ_b is equal to $2\omega_b W_b$ (W_b is a width) for $\omega_b \gg W_b$, Γ_i is intrinsic loss, and Γ_c is coupling loss. b , the modulation damping parameter, is equal to

$$b = \frac{\left(\frac{\Gamma_i}{\Gamma_c}\right)^2}{\left(1 + \frac{\Gamma_i}{\Gamma_c}\right)^2} = \left(\frac{\Gamma_i}{\Gamma_c + \Gamma_i}\right)^2. \quad (S4)$$

The bright mode Fano formula, on the other hand, is pseudo-Lorentzian and therefore symmetric, given by

$$\sigma_b(\omega) = \frac{a^2}{\left(\frac{\omega^2 - \omega_b^2}{\Gamma_b}\right)^2 + 1}. \quad (S5)$$

From Gallinet¹⁹, we find that the total optical response of the system comes from multiplying the Fano formulas of the bright mode with the dark mode modified by the bright mode, or

$$\sigma_{tot}(\omega) = \sigma_b(\omega)\sigma_a(\omega). \quad (S6)$$

Fitting our resonance to this formula, the frequency of the bright mode resonance can be extracted to determine its source, whether it be from plasma resonances of the wires, incident radiation, or Fabry-Perot resonances in the waveguide. In Supplementary Fig. 3b the Fano formula (Supplementary equation (S6)) is fit to our simulation data for a region near the resonance. All fitting parameters for Supplementary Figs. 3b-e are located in Supplementary Table 2.

The extracted bright mode from Supplementary Fig. 3b is shown in more detail in Supplementary Fig. 3c, and is compared with the normalized magnitude of the electric field at the top of a 50 nm of SiO₂/100 nm of SiN_x waveguide without wires due to Fabry-Perot resonances.

The minor misalignment of the bright mode and Fabry-Perot peak is likely caused by the grating itself altering the location of the bright mode, as the effective index of the photonic crystal made up of the grating plus the waveguide will be different than the index of the waveguide alone.

Using this method to compare our experimental and simulated data, we can compare differences quantitatively. Supplementary Figure 3d shows such a comparison. Supplementary Figure 3e plots the simulation and experimental bright modes from Supplementary Fig. 3d along with the Fabry-Perot resonance for a waveguide-only structure. If we compare the various values of the fitting parameters from Supplementary Table 2, we note that b , the modulated damping term, is higher in the experiment than in the simulation. From Supplementary equation (S4), we can see that this indicates the intrinsic loss has a larger influence (or the coupling loss has a lesser influence) in the experiment than in the simulation. This could be attributed to a , the bright mode amplitude, having a higher magnitude in the simulation than in the experiment.

Supplementary Note 3. Angle/geometry dependence of guided mode resonance structure

The absorption maxima of our wires structures are somewhat insensitive to wire height above 40 nm, and rather sensitive below, as illustrated via full wave simulations in Supplementary Fig. 4c. In contrast, the angle of incidence of light (away from normal incidence) has a very large effect on the absorption profile by splitting the single peak into two, as we can see in Supplementary Figs. 4a,b.

Supplementary Note 4. Dielectric functions of antimony telluride and bismuth telluride

Supplementary Figure 5 shows the dielectric functions of our thin-film bismuth telluride and antimony telluride materials measured using J.A. Woollam Co. VASE and IR-VASE MARK II ellipsometers and analyzed with WVASE software.

Supplementary Note 5. Absorption simulations and fitting

The values for the width, pitch, and incident illumination angle for the experiment and simulations in Fig. 3d in the main text are shown in Supplementary Table 2. $Pitch_s$ and $Width_s$ of our fabricated structures was found via SEM imaging and were used in simulations for absorption spectra (red line in Fig. 3d). Θ_s was a best fit incident illumination angle from simulation. $Pitch_f$, $Width_f$, and Θ_f were dimensions and incident illumination angle used in a simulation to best fit the experimental data. The best-fit simulation was multiplied by a scaling factor to further fit.

Supplementary Note 6. Responsivity from focused versus uniform illumination

Supplementary Figure 6 compares responsivity and noise characteristics for a Bi_2Te_3 - Sb_2Te_3 structure under focused illumination (a $60\ \mu\text{m} \times 5\ \mu\text{m}$ spot size illuminating a few single wires in the center of the array, Supplementary Fig. 6e) and spatially uniform illumination (a $120\ \mu\text{m} \times 100\ \mu\text{m}$ spot size which completely uniformly illuminated the entire structure, including the pads, Supplementary Fig. 6d) over a range of angles off normal incidence, with $\pm 1^\circ$ error, and with electric field polarized perpendicular to the wires. An objective with numerical aperture 0.14 was used for all measurements. Responsivity of the spatially uniform illumination was relative to the power incident on the area of the wires only. The unfocused, spatially uniform beam lead to a higher responsivity at nearly every wavelength than that of the focused beam, and exhibited a lineshape which more closely followed the absorption lineshape in Fig. 4a, and has similar shape and magnitude to our simulated values shown in Supplementary Fig. 8g-i (simulated absorption and thermal simulation) and Supplementary Fig. 8j-l (experimental absorption and thermal simulation). We believe the discrepancy between absorption and responsivity lineshape under focused illumination arises from uneven heating of the wire array. Because our wires are very

optically lossy (see the non-negligible imaginary dielectric constant in Supplementary Fig. 5), light diffracted into a waveguide mode by light focused on the center wires will not propagate far, and therefore wires on the edge of the structure will not absorb (or heat up) as much as wires in the center of the array. The wires with minimal temperature gradient provide a leakage pathway for thermoelectric currents, reducing responsivity and altering responsivity spectra. Spatially uniform illumination will heat the wires more equally, largely eliminating these effects.

Leakage currents from uneven heating could cause the larger noise spectral density (NSD) under focused illumination, seen in Supplementary Fig. 6b. While this NSD is convoluted with the input laser power (shown in Supplementary Fig. 9) at each wavelength, attempts to normalize NSD to Johnson noise of a temperature rise for a given power input (using knowledge that temperature rise is linear with power input, shown in Fig. 4d) did not yield a flat NSD spectra. Therefore, excess NSD must be due to noise sources which do not vary as $T^{1/2}$, as Johnson noise does. Shot noise, on the other hand, is proportional to the magnitude of the currents in a structure, and is a possible noise source arising from these back currents. The NEP is lower for nearly every wavelength for the uniform illumination, and gives detectivity values in the $1\text{-}3 \times 10^8 \text{ Hz}^{1/2}/\text{W}$ range.

Supplementary Note 7. Chromel-alumel structure results.

Thermoelectric potential (TEV) and absorption results for a chromel - alumel structure with the same dimensions as that of the bismuth telluride structures is shown in Supplementary Fig. 7. The structure is shown under $70.92 \mu\text{W}$ illumination, or $30.4 \text{ W}/\text{cm}^2$ incident power density. The focused beam is raster scanned across the wire junction region of the detector, and at each location, a data point is taken (over a $\sim 400 \mu\text{m}^2$ area). All data points are averaged together.

Supplementary Note 8. Bismuth telluride and antimony telluride compositional and structural analysis and materials characterization

Supplementary Figure 13 shows XRD data (see Methods) on thin films of Bi_2Te_3 and Sb_2Te_3 , deposited using the same protocol as for the devices in the main text. We notice that in both cases the data show signatures of nanocrystallinity or perhaps even amorphous structure in the case of antimony-telluride.

Supplementary Figure 14 shows XPS survey spectra (see Methods) for our Bi_2Te_3 and Sb_2Te_3 thin films, and due to surface sensitivity of the technique, these represent only the top few nanometers of the sample. Apart from expected surface oxidation and hydrocarbons from air, there are no other contaminants present that could affect the Seebeck coefficient. The stoichiometry of bismuth telluride and antimony telluride greatly affects the Seebeck coefficient²⁻⁴. Bismuth telluride is particularly sensitive: a small variation in atomic percent composition is capable of changing the carrier type from electrons to holes².

Using quantitative analysis based on Te 3d and Bi 4f levels, shown in Supplementary Fig. 15, we determined that the composition of our bismuth telluride was 42.5%:57.5%, Bi:Te for surface relative concentrations. This corresponds to a wt% of about 53.7% for the bismuth.

The XPS measured composition of our 50 nm antimony telluride film was determined from Sb 3d 3/2 and Te 3d 3/2 peak areas (as identified to belong to the compound), and indicates a composition of 32%:68% Sb:Te. A large amount of antimony on the surface had oxidized.

Seebeck measurements at room temperature were performed using a thin film Seebeck measurement technique described in the literature²¹. The sample thermoelectric materials were deposited on 500 nm layer of SiO_2 on a 1 cm by 1 cm silicon chip. The thermoelectric materials were of the same thickness of the structures used in this paper. Copper blocks were placed with thermally conductive paste on the hot and cold sides of a thermoelectric heating stage with the thin-film sample straddling the copper blocks, attached with thermally conductive paste. Thin K-type thermocouple wire junctions were placed on the surface of the thermoelectric material on the hot and cold ends, using physical pressure. Soldering or using thermally conductive paste to connect the wires to the samples was not recommended²¹, and we measured large hysteresis when using thermally conductive paste. A voltmeter (Keithley 6430 sub-femtoamp remote source meter) was attached to the chromel end termination of each thermocouple before it was passed into a temperature meter, providing temperature and voltage data from the exact same location on the sample. Stage temperature was measured using a build-on thermocouple attached to the stage, which roughly verified the sample temperature measurements were in the correct range. Next, the Seebeck coefficient of the chromel wire used as half of the thermocouple/electrode was measured in a similar manner to subtract out its contribution to the thin film voltage measured. Data from several specimens of each material were collected, and is displayed in Supplementary Table 3.

Variability among specimens deposited at the same time in the same chamber can be accounted for by distribution of substrate positions within the deposition system. There was no substrate rotation during the deposition, which leads to small thickness variations or unequal substrate temperatures amongst our samples. Amorphous thin films of Sb_2Te_3 have shown a variation of $100 \mu\text{V/K}$ when deposited under the same conditions⁷, indicating that our small sample-to-sample variation is not unique.

Seebeck coefficient is theoretically determined primarily by crystal band structure. For quintuple layers (unit of Te-Bi-Te-Bi-Te or Te-Sb-Te-Sb-Te) of bismuth telluride and antimony telluride, it has been calculated that band structures will be altered for less than 12 quintuple layers, due to opening of a bandgap attributed to topological surface-states, but this gap will close with more than 12 quintuple layers and approaches the bulk value²². One quintuple layer is approximately 1.1 nm (Ref. 22), putting our materials at roughly 36 quintuple layers, albeit disordered in our case. Therefore, we would not expect surface states to significantly alter the bandstructure, and therefore, the Seebeck coefficient in our 130 nm by 40 nm wires from the Seebeck coefficient in our 40 nm thick films. Our thermal simulations combined with our experimentally measured voltage support this theory. Furthermore, in a study on thin film Sb_2Te_3 , it was found that while resistivity increased with decreasing film thickness (from 790 nm to 160 nm), the film thickness had little effect on the Seebeck coefficient²³, which approaches our thickness value of 40 nm.

Bi_2Te_3 and Sb_2Te_3 have been extensively studied and characterized. As with other thermoelectric materials, the Seebeck coefficient has been found to depend heavily on deposition method and deposition temperature, as well as post-deposition treatment, such as annealing^{15,24,25}. Our Seebeck coefficients fall within the range of those found in the literature, a very small subset of which is shown in Supplementary Table 4. The ranges of Seebeck coefficient for Bi_2Te_3 in this table range from $+160 \mu\text{V/K}$ to $-228 \mu\text{V/K}$, depending on deposition method, percent Te, and oxide content. Our measured Bi_2Te_3 samples lie well within this range. Comparing our measured values to any of the values in the literature is difficult, as we were not able to determine the substrate temperature during deposition. As sputterers have different working distances and different deposition powers can be used, the substrate heating would be different in each sputterer or evaporator unless substrate heating controls are used. Sb_2Te_3 in Supplementary Table 4 ranges

in Seebeck coefficient from +70 $\mu\text{V/K}$ to +800 $\mu\text{V/K}$. Of note, noncrystalline Sb_2Te_3 (Ref. 7) has a higher Seebeck coefficient, $\sim 700\text{-}800$ $\mu\text{V/K}$. Our samples are nearly noncrystalline, based on our XRD data (Supplementary Fig. 13). Also, in this paper, two different samples deposited in the same way had a difference in Seebeck coefficient of about 100 $\mu\text{V/K}$, showing the variability in Seebeck coefficients among similar thin film samples.

The resistivities of our materials were found by measuring cloverleaf samples in a DC hall measurement system with short time constants, and showed very small error. We found a resistivity of $2.75 \times 10^{-2} \pm 7.2 \times 10^{-5}$ $\Omega\cdot\text{cm}$ for Bi_2Te_3 and $4.27 \times 10^{-1} \pm 1.1 \times 10^{-3}$ $\Omega\cdot\text{cm}$ for Sb_2Te_3 . A subset of literature resistivity values, shown in Supplementary Table 4, vary between 1.71×10^{-3} $\Omega\cdot\text{cm}$ to 8.71×10^{-3} $\Omega\cdot\text{cm}$. Our resistivity is higher than these values, but our films are much thinner and surface oxidation could play a significant role in decreasing conductivity. A subset of literature values (Supplementary Table 4) show 1.11 $\Omega\cdot\text{cm}$ to 1.04×10^{-3} $\Omega\cdot\text{cm}$ resistivities for various thin film thicknesses and deposition methods for antimony telluride. Our values lie within the literature range, closer to the values of amorphous films. Additionally, it was found that resistivity increases with decreasing film thickness in Sb_2Te_3 (Ref. 23). As our films are thinner than many in the literature, a higher resistivity, similar to ours, is expected.

We expect resistivity to be the same in our structures as in our wires, as the crystal grain sizes are small in both. Using our measured resistivity, the power factors for Sb_2Te_3 are 1.1×10^{-5} – 1.6×10^{-5} $\text{W/K}^2\cdot\text{m}$ and for Bi_2Te_3 2.2×10^{-5} – 3.3×10^{-5} $\text{W/K}^2\cdot\text{m}$. Using the literature values of thermal conductivity used in our thermal simulations (see Supplementary Note 1), this would give us zT values in the 10^{-3} – 10^{-4} range, indicating that our materials could be further optimized.

Supplementary Note 9. Analyzing D^* in our structures

By definition, $D^* = \sqrt{A} \cdot D$, where D^* is selective detectivity, A is detector area, and D is detectivity. Detectivity is defined as $D = \frac{1}{NEP}$, where NEP , or noise equivalent power, is defined as $NEP = \frac{NSD}{r}$, where r is responsivity, or the output voltage over the input power, and NSD is the noise spectral density, with a Johnson noise floor of $NSD_{Johnson} = \sqrt{4Rk_bT}$, where R is the structure resistance, k_b is the Boltzmann constant, and T is temperature. In the following calculations, we ignore shot noise from emf-induced currents, and examine the minimum D that

can be found assuming only Johnson noise. This is a reasonable approximation, given that our experimental NSD is very close to the Johnson noise limit (Fig. 4f and caption), indicating Johnson noise is the dominant noise source. The temperature differences between the pad edges and wire centers should be similar between a thermopiled structure (Supplementary Fig. 10a), and our non-thermopiled structure (Fig. 1a), indicating we can study r , D , and D^* only as a function of resistance and dimension.

Using the relations above, we find

$$D = \frac{r}{NSD} = \frac{r_1(l)}{\sqrt{\frac{4R}{n}k_bT}} \sim \sqrt{\frac{n}{R}} r_1(l), \quad (S7)$$

for a guided mode resonance wire structure shown in Fig. 1a with n wires in a parallel (non-thermopile) configuration, where R is the resistance of a single wire (so $R_{total} = \frac{R}{n}$), and $r_1(l)$ is the responsivity of a single wire. We assume that $r_1(l)$, for wires of fixed cross-sectional area and with fixed, uniform thermal conductivity, is some function of the wire length (See Supplementary Fig. 1e, for example). Assuming the majority of resistance comes from the wires (not the pads), and the cross-sectional area of the wires are constant and resistivity is the same for all wires, $R \sim l$, where l is the length of the wire. Thus, $D \sim \sqrt{\frac{n}{l}} r_1(l)$. The total detector area of the structure (counting the wire area only), is approximately $A = nlp$, where p is the pitch of the wires. Then,

$$D^* \sim \sqrt{nlp} \cdot \sqrt{\frac{n}{l}} r_1(l) = n\sqrt{p} r_1(l) = \frac{np r_1(l)}{p^{\frac{1}{2}}} = \text{structure width} \times \frac{r_1(l)}{p^{\frac{1}{2}}}. \quad (S8)$$

Structure width and $r_1(l)$ are independent of one another and will not cancel in general. Therefore, D^* will not give a detection figure of merit independent of area and is not a good metric for our structures. Other thermal detectors have similar problems using D^* as a figure of merit²⁶.

For a thermopiled device of n wires, where the wires are in series, i.e. total resistance $R_{total} = nR$, the detectivity (D_{TP}) is

$$D_{TP} = \frac{r_{TP}}{NSD} = \frac{nr_1(l)}{\sqrt{4nRk_bT}} \sim \frac{nr_1(l)}{\sqrt{nR}} = \sqrt{\frac{n}{R}} r_1(l) \sim \sqrt{\frac{n}{l}} r_1(l), \quad (S9)$$

which is the same as detectivity for a thermocouple (Supplementary Eq. (S7)), again neglecting contributions of the pads to resistance. Since the detector area is the same for thermopiled and non-thermopiled structures, then D^* will also be the same.

Supplementary Note 10. Calculating responsivity and detectivity with state-of-the-art materials.

Large responsivity and low noise are needed to have high detectivity. Larger responsivity arises from a higher Seebeck coefficient, α , and a larger temperature gradient (therefore, smaller thermal conductivity, k). Lower Johnson noise (the primary noise source in our structure, shown in Fig. 4f), comes from lower resistance, and therefore lower resistivity, ρ . Thus, detectivity can be improved with a higher thermoelectric figure of merit, $zT = \frac{\alpha^2 T}{\rho k}$, material. At room temperature, one of the best p-type materials is a BiSbTe alloy which has a zT of 1.2 at room temperature²⁷. One of the best performing n-type materials is a PbSeTe quantum dot superlattice material with a zT of 1.3-1.6 at room temperature²⁸. The resistivity of the high zT materials are $1.71 \times 10^{-3} \Omega \cdot \text{cm}$ (n-type) and $8.00 \times 10^{-4} \Omega \cdot \text{cm}$ (p-type), the thermal conductivities are $0.58 \text{ W/m} \cdot \text{K}$ (n-type) and $1.1 \text{ W/m} \cdot \text{K}$ (p-type), and the Seebeck coefficients are $-219 \mu\text{V/K}$ (n-type) and $185 \mu\text{V/K}$ (p-type). While we did not measure the thermal conductivity of our materials, assuming bulk values¹¹ of thermal conductivity for our Bi_2Te_3 ($\sim 2.05 \text{ W/m} \cdot \text{K}$) and Sb_2Te_3 ($\sim 3.54 \text{ W/m} \cdot \text{K}$), we can see that the overall thermal conductivity with the high zT materials would be decreased by a factor of ~ 4 . While our thermal simulations were able to explain experimental results reasonably well (compare Supplementary Fig. 8g-l and Fig. 4b), it is known that small crystal grain sizes can decrease thermal conductivity in thin film BiTe-based materials¹⁵. From our XPS data (Supplementary Fig. 13), we can see that the grain sizes must be small. This indicates that our thermal conductivity may not be greatly improved by using the state-of-the-art materials above. In results from thermal simulations we can see that using state-of-the-art n-type material, shown in Supplementary Fig. 8d-f, versus our n-type Bi_2Te_3 material, shown in Supplementary Fig. 8g-i, we get $\sim 40\%$ increase in responsivity. Our structures depend both on the thermal conductivity of the thermoelectric material, and the thermal conductivity of the substrate. Fortunately, suspended low-stress SiN_x membranes¹³ and SiO_2 can have thermal conductivities lower than or similar to

the thermoelectric materials we study. To remove the thermal conductivity contribution from the substrate, the substrate could be etched from beneath the wires, although this would affect the optical absorption characteristics.

The Seebeck coefficient for the large zT n-type material are larger than ours by a factor of 2.6 ($-219 \mu\text{V/K}$ versus an average of $-84 \mu\text{V/K}$), and the Seebeck coefficients for the large zT p-type material were smaller than our materials by a factor of ~ 1.3 ($185 \mu\text{V/K}$ versus an average of $242 \mu\text{V/K}$). This gives an overall Seebeck coefficient of $404 \mu\text{V/K}$ for the optimal materials, versus $326 \mu\text{V/K}$ for our materials, or a factor of ~ 1.24 increase in Seebeck coefficient. The resistivity of the large zT n-type material decreases by a factor of 16 over our n-type material resistivity ($1.71 \times 10^{-3} \Omega \cdot \text{cm}$ versus $2.75 \times 10^{-2} \Omega \cdot \text{cm}$), and the resistivity of the large zT p-type material decreases by a factor of 534 over our p-type material resistivity ($8.00 \times 10^{-4} \Omega \cdot \text{cm}$ versus $4.27 \times 10^{-1} \Omega \cdot \text{cm}$). We can treat our system as two resistors in series, one resistor composed of n-type material and the other composed of p-type material. Then, assuming a symmetric system, the total resistance is proportional to the sum of the resistivities of the two materials. The sum of the resistivities of the Bi_2Te_3 and Sb_2Te_3 materials in our paper is $4.55 \times 10^{-1} \Omega \cdot \text{cm}$, and the sum of the resistivities of the state-of-the-art materials is $2.51 \times 10^{-3} \Omega \cdot \text{cm}$. Thus, resistance decreases by a factor of about 181 from our materials to the state-of-the-art. While nanostructuring could change the material properties of the high zT materials, an approximation for the expected detectivity increase can still be found.

Based on our simulations, a factor of 4 decrease in thermal conductivity in our Thermoelectric materials will produce a factor of 1.4 increase in temperature difference between the hot and cold end of our device. Coupled with a factor of 1.24 increase in Seebeck coefficient, we can expect the responsivity to increase by a factor of ~ 1.7 using the state-of-the-art thermoelectric materials. Noise spectral density depends on the square root of resistance (assuming Johnson noise dominates), so decreasing resistance by a factor of 181 will lead to a decrease in noise by about a factor of 13. Therefore, the detectivity can be increased by around $1.7 \times 13 = \sim 22$ times by using state-of-the-art thermoelectric materials.

Supplementary Note 11. Noise characteristics of other resonant absorbing structures.

The designs studied in Supplementary Fig. 10c,d and Supplementary Figs. 11,12 theoretically could have higher detectivities than the guided mode resonance wire structures described and tested in the manuscript. For the perfect absorber (Supplementary Fig. 10c) and split ring resonator absorbers (Supplementary Fig. 10d), we have designed a thermal management scheme to provide motivation for future research. The nanophotonic absorber arrays were placed in the center of a thin thermoelectric junction on top of a thin membrane of SiN_x , described further in Supplementary Fig. 10j, Supplementary Fig. 12, and Supplementary Note 1. The simulation was done without any assumed thermal convection in the surrounding ambient. The supporting edges of the thermoelectric ‘bridge’ structure depicted in Supplementary Fig. 12 were placed on a laminate of SiN_x on a thin Au film on a thick layer of SiO_2 . The high thermal conductivity of the thin Au layer greatly lowered the “cold side” temperature of the thermoelectric material to near room temperature, compared to when this layer was not present. This allowed us to increase the thermal gradient within the thermoelectric materials, creating higher responsivities than in our resonant wire structures, from 180 to 390 V/W (Supplementary Fig. 10m,n). Using the measured resistivities for our structures, ($2.75 \times 10^{-2} \pm 7.2 \times 10^{-5} \text{ } \Omega \cdot \text{cm}$ for Bi_2Te_3 and $4.27 \times 10^{-1} \pm 1.1 \times 10^{-3} \text{ } \Omega \cdot \text{cm}$ for Sb_2Te_3 , found in Supplementary Note 8) and the dimensions described in Supplementary Fig. 12, the resistance of the thermoelectric element would be around 91 k Ω in the perfect absorber, and 152 k Ω in the split ring resonator, giving a theoretical Johnson noise of 38 nV/Hz^{1/2} and 50 nV/Hz^{1/2}, respectively. Thus, the minimum noise equivalent power (NEP) would be 0.2 nW/Hz^{1/2} for the perfect absorber and 0.13 nW/Hz^{1/2} for the split ring resonator absorber, shown in Supplementary Fig. 11h,i. This is 10 to 20 times less than our measured and simulated NEP minima of our structures, which is significant.

Supplementary Note 12. Resonant thermoelectric nanophotonics versus conventional thermoelectric detectors.

The distinction between a conventional (c.f. Ref. 29) thermopile and a resonant thermopile (Supplementary Fig. 10a) lies in the total heat capacity of the hot end of the structure. A smaller heat capacity (i.e. smaller structure) will generally have both higher responsivity and smaller time constant for the same amount of incident power absorbed. Resonant absorbing structures can absorb a large fraction of light in small volumes because their absorption cross-section is much

larger than their geometric cross-section, unlike conventional absorbing layers such as black paint. Furthermore, layers like black paint, which rely on single-pass material absorption, need to be thicker than the skin depth of the incident light, whereas this is not a requirement for resonant structures which rely on multiple-passes of light. If the thermopile detector takes advantage of absorption from multiple passes of light with non-thermoelectric absorbers³⁰, the heat capacity for this structure will still be higher than if the thermoelectric materials themselves were the absorbers, and still gives a 10's of ms time constant, as there is simply more material if an absorber plus a thermoelectric element is needed. Thus, if equal amounts of light are absorbed, thermoelectric structures which themselves absorb (especially suspended, isolated thermoelectric absorbers) have the potential for higher responsivity with lower time constant than devices with non-thermoelectric absorbing structures, because of the smaller volume and therefore heat capacity of the materials involved.

Take as an example the thermopile structure in Ref. 29. This structure relies on an absorbing layer on the order of microns thick and 500 μm in diameter inside a circle of thermopiles. If we have the guided mode resonant thermoelectric thermopile structure shown in Supplementary Fig. 10a that uses thermoelectric material as the absorber, and assume the thermoelectric materials absorb an equivalent amount as the membrane, then the maximum temperature will occur in the thermoelectric wires themselves, but with much less material than in the membrane in Ref. 29. This will lead to a higher responsivity and lower time constant in the resonant thermoelectric structure, although the noise spectral density may be higher due to larger resistance in the structure. Our present design has an absorption maximum of about 60% in the thermoelectric wires, but by altering the design slightly to form a Salisbury screen³¹, 100% absorption can be reached in the thermoelectric materials.

Supplementary References

- 1 Gallinet, B. & Martin, O. J. F. Influence of electromagnetic interactions on the line shape of plasmonic fano resonances. *ACS Nano* **5**, 8999-9008 (2011).
- 2 Horne, R. A. Effect of oxide impurities on the thermoelectric powers and electrical resistivities of bismuth, antimony, tellurium, and bismuth-tellurium alloys. *J. Appl. Phys.* **30**, 393-397, (1959).
- 3 Bottner, H. *et al.* New thermoelectric components using microsystem technologies. *J. Microelectromech. S* **13**, 414-420 (2004).

- 4 da Silva, L. W., Kaviany, M. & Uher, C. Thermoelectric performance of films in the bismuth-tellurium and antimony-tellurium systems. *J. Appl. Phys.* **97**, 114903 (2005).
- 5 Zou, H. L., Rowe, D. M. & Williams, S. G. K. Peltier effect in a co-evaporated $\text{Sb}_2\text{Te}_3(\text{P})\text{-Bi}_2\text{Te}_3(\text{N})$ thin film thermocouple. *Thin Solid Films* **408**, 270-274 (2002).
- 6 Pinisetty, D., Gupta, M., Karki, A. B., Young, D. P. & Devireddy, R. V. Fabrication and characterization of electrodeposited antimony telluride crystalline nanowires and nanotubes. *J. Mater. Chem.* **21**, 4098-4107 (2011).
- 7 Baily, S. A. & Emin, D. Transport properties of amorphous antimony telluride. *Phys. Rev. B* **73**, 165211 (2006).
- 8 Shi, W. D., Zhou, L., Song, S. Y., Yang, J. H. & Zhang, H. J. Hydrothermal synthesis and thermoelectric transport properties of impurity-free antimony telluride hexagonal nanoplates. *Adv. Mater.* **20**, 1892 (2008).
- 9 Gorbachuk, N. P., Bolgar, A. S., Sidorko, V. R. & Goncharuk, L. V. Heat capacity and enthalpy of Bi_2Si_3 and Bi_2Te_3 in the temperature range 58-1012 K. *Powder Metall. Met. C+* **43**, 284-290 (2004).
- 10 Nolas, G. S., Sharp, J. & Goldsmid, H. J. *Thermoelectrics : Basic Principles and New Materials Developments* (Springer, 2001).
- 11 Rowe, D. M. & Bhandari, C. M. *CRC Handbook of Thermoelectrics* (CRC, 1995).
- 12 Greenwood, N. N. & Earnshaw, A. *Chemistry of the Elements* (Pergamon Press, Inc., 1984).
- 13 Ftouni, H. *et al.* Thermal conductivity of silicon nitride membranes is not sensitive to stress. *Phys. Rev. B* **92**, 125439 (2015).
- 14 Yamane, T., Nagai, N., Katayama, S. & Todoki, M. Measurement of thermal conductivity of silicon dioxide thin films using a 3 omega method. *J. Appl. Phys.* **91**, 9772-9776 (2002).
- 15 Takashiri, M. *et al.* Effect of grain size on thermoelectric properties of n-type nanocrystalline bismuth-telluride based thin films. *J. Appl. Phys.* **104**, 084302 (2008).
- 16 Palik, E. D. *Handbook of Optical Constant of Solids* (Academic Press, 1997).
- 17 Liu, N., Mesch, M., Weiss, T., Hentschel, M. & Giessen, H. Infrared perfect absorber and its application as plasmonic sensor. *Nano Lett.* **10**, 2342-2348 (2010).
- 18 Johnson, P. B. & Christy, R. W. Optical constants of the noble metals. *Phys. Rev. B* **6**, 4370-4379 (1972).
- 19 Gallinet, B. *Fano resonances in plasmonic nanostructures: Fundamentals, numerical modeling and applications*, PhD thesis, EPFL (2012).
- 20 Gallinet, B. & Martin, O. J. F. Relation between near-field and far-field properties of plasmonic Fano resonances. *Opt. Express* **19**, 22167-22175 (2011).
- 21 Singh, R. & Shakouri, A. Thermostat for high temperature and transient characterization of thin film thermoelectric materials. *Rev. Sci. Instrum.* **80**, 025101 (2009).
- 22 Sung, J. H. *et al.* Atomic layer-by-layer thermoelectric conversion in topological insulator bismuth/antimony tellurides. *Nano Lett.* **14**, 4030-4035 (2014).
- 23 Rajagopalan, N. S. & Ghosh, S. K. Measurements of some electrical and thermoelectrical properties of antimony telluride films. *Physica* **29**, 234 (1963).
- 24 Kim, D. H. & Lee, G. H. Effect of rapid thermal annealing on thermoelectric properties of bismuth telluride films grown by co-sputtering. *Mat. Sci. Eng. B-Solid* **131**, 106-110 (2006).
- 25 Rashid, M. M., Cho, K. H. & Chung, G. S. Rapid thermal annealing effects on the microstructure and the thermoelectric properties of electrodeposited Bi_2Te_3 film. *Appl. Surf. Sci.* **279**, 23-30 (2013).
- 26 Driggers, R. G. *Encyclopedia of Optical Engineering*. Vol. 1, 351 (Marcel Dekker, 2003).
- 27 Poudel, B. *et al.* High-thermoelectric performance of nanostructured bismuth antimony telluride bulk alloys. *Science* **320**, 634-638 (2008).
- 28 Harman, T. C., Taylor, P. J., Walsh, M. P. & LaForge, B. E. Quantum dot superlattice thermoelectric materials and devices. *Science* **297**, 2229-2232 (2002).

- 29 Volklein, F. & Wiegand, A. High-sensitivity and detectivity radiation thermopiles made by multilayer technology. *Sensor Actuat. a-Phys.* **24**, 1-4 (1990).
- 30 Gawarikar, A. S., Whea, R. P., R. P. S. & Talghader J. J. High detectivity uncooled thermal detectors with resonant cavity coupled absorption in the long-wave infrared, *IEEE Trans. Electron Devices* **16**, 2586-2591 (2013).
- 31 R.L. Fante & M.T. McCormack, Reflection properties of the Salisbury screen, *IEEE Trans. Antennas Propag.*, **36**, 10, 1443 - 1454 (1988)